PHYSICAL REVIEW C **95**, 065805 (2017)

# Structure of neutron star crusts from new Skyrme effective interactions constrained by chiral effective field theory

Yeunhwan Lim[1,*] and Jeremy W. Holt[1,2,†]
[1]*Cyclotron Institute, Texas A&M University, College Station, Texas 77843, USA*
[2]*Department of Physics and Astronomy, Texas A&M University, College Station, Texas 77843, USA*
(Received 9 February 2017; revised manuscript received 12 May 2017; published 30 June 2017)

We investigate the structure of neutron star crusts, including the crust-core boundary, based on new Skyrme mean field models constrained by the bulk-matter equation of state from chiral effective field theory and the ground-state energies of doubly-magic nuclei. Nuclear pasta phases are studied using both the liquid drop model as well as the Thomas-Fermi approximation. We compare the energy per nucleon for each geometry (spherical nuclei, cylindrical nuclei, nuclear slabs, cylindrical holes, and spherical holes) to obtain the ground state phase as a function of density. We find that the size of the Wigner-Seitz cell depends strongly on the model parameters, especially the coefficients of the density gradient interaction terms. We employ also the thermodynamic instability method to check the validity of the numerical solutions based on energy comparisons.

DOI: 10.1103/PhysRevC.95.065805

## I. INTRODUCTION

Neutron stars offer the possibility to study matter under extreme conditions (in density and neutron-to-proton ratio) inaccessible to laboratory experiments on Earth. The inner core of a neutron star may reach densities as high as five to ten times nuclear saturation density, a regime for which no well-converged theoretical expansions are presently available. The structure and composition of the inner core are consequently highly uncertain and may contain deconfined quark matter [1–3], hyperonic matter [4–8], or meson condensates [9–12]. In contrast, the inner crust and outer core span densities from $n \simeq 4 \times 10^{11}$ to $5 \times 10^{14}$ g/cm$^3$, corresponding to nucleon Fermi momenta of $k_F \lesssim 400$ MeV, which are much less than the chiral symmetry breaking scale of $\Lambda_\chi = 4\pi f_\pi \simeq 1$ GeV. Chiral effective field theory (EFT) [13] may therefore provide a suitable theoretical framework for exploring neutron star matter at these densities.

In recent years there has been significant progress in the development of realistic chiral nucleon-nucleon (NN) forces [14–17] at and beyond next-to-next-to-next-to-leading order (N3LO) in the chiral power counting. Nuclear many-body forces become relevant in homogeneous matter at densities larger than $n \gtrsim 0.25 n_0$ (where $n_0 = 2.4 \times 10^{14}$ g/cm$^3$ is the saturation density of nuclear matter) and have been included in numerous studies of the cold nuclear and neutron matter equations of state (EOS) [18–28]. Neutron star structure and evolution requires in addition the equation of state at arbitrary isospin-asymmetry [29,30] and finite temperature [31–33], which has been computed consistently with the same chiral nuclear force models and many-body methods. The inhomogeneous phase of nuclear matter encountered in neutron star crusts depends also on gradient contributions to the energy density. Previous work has focused on the leading-order Hartree-Fock contribution to the isoscalar and isovector gradient couplings from the density matrix expansion [34–36], *ab initio* studies of the isovector gradient coupling strength from quantum Monte Carlo simulations of pure neutron matter [37,38], and nuclear response functions in Fermi liquid theory [39–42].

Neutron star crusts have been studied using phenomenological liquid drop models [43–45] and the Thomas-Fermi approximation [46–51]. Nuclear pasta phases resulting from the competition between the Coulomb interaction and nuclear surface tension were also treated in the liquid drop and Thomas-Fermi methods. More sophisticated approaches to the nuclear pasta phase have been investigated using the Skyrme-Hartree Fock approximation [52–55] and molecular dynamics simulations [56–58].

In the present work we utilize recent results for the homogeneous nuclear matter equation of state from chiral EFT to develop new Skyrme mean field parametrizations that enable the study of finite nuclei, inhomogeneous nuclear matter in neutron star crusts, and the mass-radius relation of neutron stars. Recent works [59–61] have used the low-density equation of state of neutron matter from chiral EFT to constrain nonrelativistic and relativistic mean field models, while the present study includes the full isospin-asymmetric matter equation of state at second order in perturbation theory up to $n = 2n_0$ as a fitting constraint. Several chiral nuclear force models are considered in order to estimate the theoretical uncertainty.

We find that the traditional Skyrme model cannot accommodate the density dependence of the nuclear equations of state derived from chiral effective field theory ($\chi$EFT). We therefore introduce additional interaction terms in the Skyrme Hamiltonian that go as the next higher power of the Fermi momentum. This enables an accurate reproduction of the bulk-matter equation of state from chiral EFT. Using the new models, we investigate the phase of subsaturation nuclear matter, which is expected to be present at the boundary between the outer core and inner crust of neutron stars, an environment that is highly neutron rich. Indeed the proton fraction of nuclear matter in beta equilibrium at the crust-core boundary is roughly

---

[*] ylim@tamu.edu
[†] holt@physics.tamu.edu

∼3%. In the boundary region, nuclear matter experiences a shape change caused by the competition between the repulsive Coulomb interaction and surface tension. We adopt the analytic solution of the Coulomb interaction in discrete dimensions to study the phase of nuclear matter in the liquid drop model (LDM) formalism. The energy per nucleon of nuclear matter determines the lowest energy state and therefore the discrete shape in the pasta phase. We also study inhomogeneous nuclear matter by employing the Thomas-Fermi (TF) approximation employing a parameterized density profile (PDP) for neutrons and protons.

The paper is organized as follows. In Sec. II we describe the Skyrme force model used to investigate the neutron star inner crust and outer core. The traditional Skyrme model is extended in order to reproduce the homogeneous matter equation of state of isospin-asymmetric nuclear matter from chiral effective field theory as well as the ground state energies of doubly-magic nuclei. In Sec. III, we present the numerical method to determine the transition density for the core-crust boundary. The liquid drop model, Thomas-Fermi approximation, and thermodynamic instability methods are then employed to find the transition densities. We summarize our results in Sec. IV.

## II. NUCLEAR MODEL

We begin by describing the microscopic chiral nuclear force models [24,62] employed in the present study. The two-body force is treated at N3LO in the chiral expansion, and the 24 low-energy constants associated with NN contact terms are fitted to elastic nucleon-nucleon scattering phase shifts and deuteron properties. The three-body force is treated at N2LO, and the $c_E$ and $c_D$ low-energy constants associated with the contact three-body force and one-pion exchange three-body force, respectively, are fitted to reproduce the ground-state energies of $^3$H and $^3$He as well as the beta-decay lifetime of $^3$H. The resolution scale is set by the momentum-space cutoff $\Lambda$, which is varied over the range $414 < \Lambda < 500$ MeV. At this resolution scale many-body perturbation theory is well converged, and the resulting neutron matter equation of state below saturation density is strongly constrained [63]. Cutoff variation provides only one means to study the theoretical uncertainties in chiral effective field theory, and future work will be devoted understanding better the errors due to neglected higher-order terms in the chiral expansion.

To be specific we use three different values of the momentum-space cutoff, $\Lambda = 414$, 450, and 500 MeV, we and denote the corresponding nuclear potentials as n3lo414, n3lo450, and n3lo500. The strategy is then to identify what approximations are needed in each case to provide an accurate description of the bulk matter equation of state in the vicinity of nuclear matter saturation. As shown in previous work [24], the chiral potentials with the two lowest cutoff values give reasonable nuclear matter properties at second order in many-body perturbation theory with Hartree-Fock intermediate-state propagators. In particular, the saturation energy lies in the range $E/A = -(15.7\text{–}16.2)$ MeV while the saturation density lies in the range $n_0 = (0.165\text{–}0.174)\ \text{fm}^{-3}$. At the same approximation in many-body perturbation theory, the $\Lambda = 500$ MeV chiral potential exhibits too little attraction, and the binding energy per nucleon at saturation density is only $E/A \simeq -11.5$ MeV. We therefore employ for this potential second-order perturbation theory with free-particle intermediate-state energies, which on the one hand accounts for theory uncertainties associated with the choice of the single-particle energy spectrum, and on the other hand leads to an improved description of nuclear matter saturation. The latter results from a larger density of states near the Fermi surface that enhances the overall attraction from the second-order perturbative contribution. In this case the saturation energy and density are $E/A = -15.9$ MeV and $n_0 = 0.171\ \text{fm}^{-3}$, respectively.

The calculations outlined above have been extended in the present work to describe cold nuclear matter at arbitrary isospin asymmetry. The resulting equations of state are then used as data in fitting new Skyrme model parametrizations. In addition, the density-gradient contributions to the nuclear energy density, which have important effects on the structure of the neutron star inner crust, are constrained by including the ground-state energies of doubly-magic nuclei in the $\chi^2$ minimization function for the Skyrme model parameters.

The same two- and three-body chiral potentials have also been used in numerous studies of nuclear dynamics and thermodynamics (for recent reviews, see Refs. [64,65]). In particular, the critical endpoint of the first-order liquid-gas phase transition line was found [32] to be consistent with recent empirical determinations [66], and the low-density–high-temperature equation of state of pure neutron matter was found [33] to be in very good agreement with the model-independent virial expansion. The applications described below focus on the cold neutron star composition and equation of state, but we may anticipate future extensions to finite temperature matter employing a strategy similar to that described above.

The energy density in dense nuclear matter can be expanded in powers of the proton and neutron Fermi momenta, $k_f^p = (3\pi^2 n_p)^{1/3}$ and $k_f^n = (3\pi^2 n_n)^{1/3}$, as follows:

$$\begin{aligned}\varepsilon = {}& \frac{1}{2m}(\tau_n + \tau_p) + \alpha_L\left(n_n^2 + n_p^2\right) + 2\alpha_U n_n n_p \\ & + \left[\eta_L\left(n_n^2 + n_p^2\right) + 2\eta_U n_n n_p\right] n^\gamma,\end{aligned} \tag{1}$$

where $\alpha_{L,U}$, $\eta_{L,U}$, and $\gamma$ are constants and

$$\begin{aligned}\tau_n &= \tfrac{3}{5}(3\pi^2)^{2/3} n^{5/3}(1-x)^{5/3},\\ \tau_p &= \tfrac{3}{5}(3\pi^2)^{2/3} n^{5/3}(1-x)^{5/3},\end{aligned} \tag{2}$$

$n_n = n(1-x)$, and $n_p = nx$. The above approximation can explain $\chi$EFT asymmetric matter results quite well with small deviation (<1%). However, it cannot be used to calculate the properties of finite nuclei directly unless we find the surface tension in the liquid drop model or the gradient terms in the Thomas-Fermi approximation

The polynomial expansion in Eq. (1) can be derived from the phenomenological Skyrme nucleon-nucleon interaction, given by [67–69]:

$$\begin{aligned} v_{i,j}(\mathbf{r}_i,\mathbf{r}_j) = {} & t_0(1+x_0P_\sigma)\delta(\mathbf{r}_i-\mathbf{r}_j) \\ & + \frac{t_1}{2}(1+x_1P_\sigma)[\delta(\mathbf{r}_i-\mathbf{r}_j)\mathbf{k}^2+\mathbf{k}'^2\delta(\mathbf{r}_i-\mathbf{r}_j)] \\ & + t_2(1+x_2P_\sigma)\mathbf{k}'\cdot\delta(\mathbf{r}_i-\mathbf{r}_j)\mathbf{k} \\ & + \frac{1}{6}t_3(1+x_3P_\sigma)\rho^{\gamma_1}\delta(\mathbf{r}_i-\mathbf{r}_j) \\ & + iW_0\mathbf{k}'\delta(\mathbf{r}_i-\mathbf{r}_j)\times\mathbf{k}\cdot(\boldsymbol{\sigma}_i+\boldsymbol{\sigma}_j), \end{aligned} \tag{3}$$

where $P_\sigma$ is the spin exchange operator, $\mathbf{k}=\frac{1}{2i}(\nabla_i-\nabla_j)$, $\mathbf{k}'=-\frac{1}{2i}(\nabla_i'-\nabla_j')$, and the local density $\rho$ is evaluated at $(\mathbf{r}_i+\mathbf{r}_j)/2$.

Traditional Skyrme force models have ten parameters which can be fitted to the binding energies of finite nuclei, neutron skin thicknesses, bulk matter properties, and neutron matter calculations. However, we find that this number of parameters is insufficient to reflect both the equation of state of asymmetric nuclear matter from chiral EFT as well as the properties of finite nuclei. We therefore extend the traditional Skyrme force model by adding extra density dependent terms of the form

$$v_{ij}\rightarrow v_{ij}+\tfrac{1}{6}t_4(1+x_4P_\sigma)\rho^{\gamma_2}\delta(\mathbf{r}_i-\mathbf{r}_j). \tag{4}$$

We determine the Skyrme Hartree-Fock parameters from fitting to the recent $\chi$EFT asymmetric nuclear matter calculations outlined in Ref. [30] together with the binding energies of doubly closed shell nuclei. We define the $\chi^2$ minimization function:

$$\begin{aligned} & \chi^2(x_0,\dots,x_4,t_0,\dots,t_4,W_0) \\ & \quad = w_b\left[\frac{1}{N_iN_j}\sum\left\{\frac{\mathcal{E}^{\mathrm{EFT}}(n_i,x_j)-\mathcal{E}^{\mathrm{Sk}}(n_i,x_j)}{\mathrm{MeV}}\right\}^2\right] \\ & \qquad + w_{n_0}(0.16-\rho_0\ \mathrm{fm}^3)^2+w_B(-16+B^{\mathrm{Sk}}\ \mathrm{MeV}^{-1})^2 \\ & \qquad + w_F\left[\frac{1}{N_k}\sum\left(\frac{B_k^{\mathrm{Exp.}}-B_k^{\mathrm{Sk}}}{\mathrm{MeV}}\right)^2\right] \end{aligned} \tag{5}$$

with weighting factors $\{w_b,w_{n_0},w_B,w_F\}$.

Since Hartree-Fock theory is the lowest order approximation in a systematic many-body perturbation theory expansion, there is no clean one-to-one correspondence between the Skyrme parameters and the chiral expansion coefficients. It is, however, possible to reproduce properties of the chiral EFT equation of state from a simplified Skyrme mean field model. The desirable aspect of the Skyrme parametrization is that it enable us to then calculate also the properties of finite nuclei, such as their density profiles and binding energies, as well as the composition and structure of neutron star inner crusts.

We present the new Skyrme parametrizations in Table I. We set $\gamma_1=1/3$ and $\gamma_2=1$ in all cases. This can be justified when we consider that the energy density of bulk nuclear matter can be expanded as a function of the Fermi momentum $k_f$. Note that $x_4$ is much larger than the other $x$'s in the parametrization. This indicates that spin exchange interactions give very large attraction in dense matter within the extended Skyrme formalism. Figure 1 shows the energy per baryon in asymmetric nuclear matter from both chiral effective field theory and Skyrme phenomenology. The "+" denotes the energy per baryon from $\chi$EFT with $\Lambda=450$ MeV, while the solid lines are results from the new Skyrme models derived in our work. The deviations get larger as the total baryon number density increases, but overall the agreement is quite satisfactory given the simplicity of the Skyrme mean field model. We have performed the same fitting procedure also for the $\Lambda=414$ MeV and $\Lambda=500$ MeV chiral nuclear potentials, and in these cases the fit is of the same quality as that shown in Fig. 1 for the case $\Lambda=450$ MeV. We include as well the total binding energy of doubly-magic nuclei in the $\chi^2$ minimization function for the Skyrme parametrizations. Table II shows the results of the Skyrme Hartree-Fock calculations compared to the experimental values [70].

TABLE I. Skyrme force parameters fitted to the chiral N3LO asymmetric matter equation of state and finite nuclei binding energies. The parameters have units such that the energy density is given in MeV fm$^{-3}$.

| | Sk$\chi$414 | Sk$\chi$450 | Sk$\chi$500 |
|---|---|---|---|
| $t_0$ | −1734.0261 | −1803.2928 | −1747.48258 |
| $t_1$ | 255.6550 | 301.8208 | 241.31968 |
| $t_2$ | −264.0678 | −273.2827 | −331.04118 |
| $t_3$ | 12219.5884 | 12783.8619 | 12491.50533 |
| $t_4$ | 556.1320 | 564.1049 | 405.03174 |
| $x_0$ | 0.4679 | 0.4430 | 0.59530 |
| $x_1$ | −0.5756 | −0.3622 | −1.15893 |
| $x_2$ | −0.3955 | −0.4105 | −0.58432 |
| $x_3$ | 0.7687 | 0.6545 | 1.20050 |
| $x_4$ | −15.8761 | −11.3160 | −25.49381 |
| $\gamma_1$ | 1/3 | 1/3 | 1/3 |
| $\gamma_2$ | 1 | 1 | 1 |
| $W_0$ | 93.7236 | 106.4288 | 98.08897 |

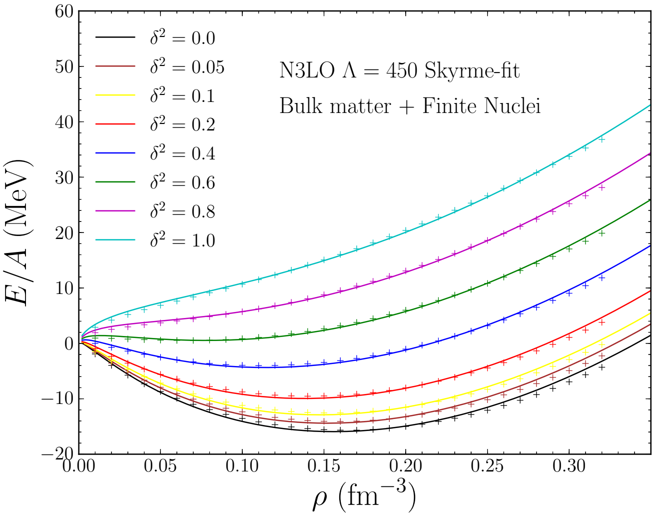

FIG. 1. Comparison of the energy per baryon in asymmetric nuclear matter from chiral EFT ($\Lambda=450$ MeV) and its Skyrme fitting model. The isospin asymmetry is denoted by $\delta=(n_n-n_p)/(n_n+n_p)$.

TABLE II. Skyrme Hartree-Fock results for the binding energies (in units of MeV) of doubly closed shell nuclei together with bulk nuclear matter properties [71].

| | Exp. | Sk$\chi$414 | Sk$\chi$450 | Sk$\chi$500 |
|---|---|---|---|---|
| $^{16}$O | 127.62 | 126.73 | 126.93 | 127.07 |
| $^{40}$Ca | 342.05 | 342.63 | 341.93 | 341.43 |
| $^{48}$Ca | 415.99 | 416.66 | 416.69 | 417.24 |
| $^{56}$Ni | 483.99 | 482.29 | 482.32 | 482.38 |
| $^{100}$Sn | 825.78 | 826.20 | 825.69 | 822.55 |
| $^{132}$Sn | 1102.90 | 1103.05 | 1103.22 | 1106.91 |
| $^{208}$Pb | 1636.44 | 1635.88 | 1636.21 | 1635.30 |
| $\rho_0$ (fm$^{-3}$) | $0.160 \pm 0.005$ | 0.1697 | 0.1562 | 0.1679 |
| $B$ (MeV) | $16.0 \pm 0.5$ | 16.1987 | 15.9262 | 15.9895 |
| $K$ (MeV) | $230 \pm 30$ | 243.19 | 239.53 | 238.16 |
| $S_v$ (MeV) | $32.5 \pm 2.5$ | 32.3456 | 30.6346 | 29.1167 |
| $L$ (MeV) | $58 \pm 18$ | 51.9307 | 42.0518 | 40.7415 |

Having determined all Skyrme model parameters from the $\chi^2$ fitting function in Eq. (5), we now check theoretical predictions for bulk matter and finite nuclei. Also in Table II we show the properties of nuclear matter around the saturation density, including the saturation energy per particle $B$, the nuclear incompressibility $K$, the isospin-asymmetry energy $S_v$, and the isospin-asymmetry slope parameter $L$. Overall the microscopic predictions agree very favorably with experimental constraints [71].

As an example of the Skyrme Hartree-Fock calculations for finite nuclei, we present the density profile of $^{208}$Pb in Fig. 2. The experimental charge density [72] is included for comparison. The central density of $^{208}$Pb from the $\Lambda = 414$ MeV and $\Lambda = 500$ MeV chiral potentials is greater than that from the $\Lambda = 450$ MeV potential model. This can be understood by noting that the saturation density of the $\Lambda = 450$ MeV model is close to the empirical value of $n_0 = 0.16$ fm$^{-3}$, while the other two potentials give saturation densities closer to $n_0 = 0.17$ fm$^{-3}$.

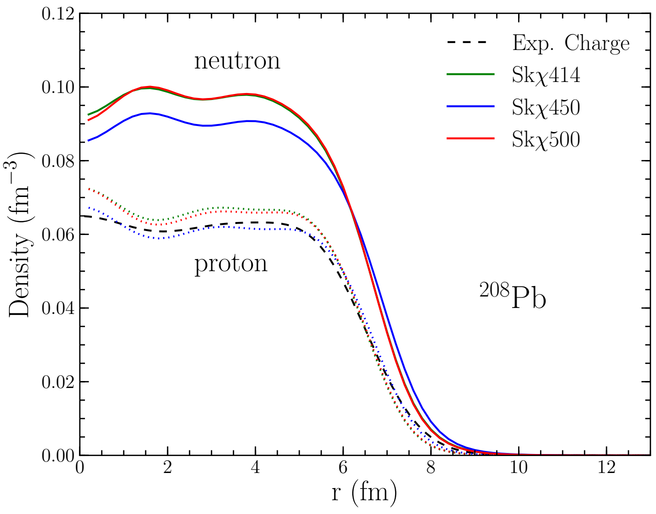

FIG. 2. Density profiles of neutron and proton in $^{208}$Pb using Skyrme Hartree-Fock calculations. Experimental charge density is also added for comparison.

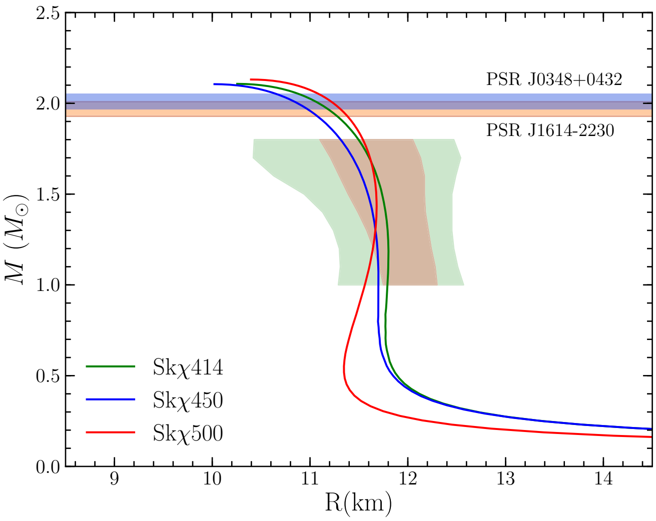

FIG. 3. Mass-radius curves from the Skyrme mean field models constructed in the present work.

To check the behavior of the Skyrme mean field models in the high-density region ($\rho > 0.4$ fm$^{-3}$), we solve the Tolman-Oppenheimer-Volkov (TOV) equations for a static cold neutron star:

$$\begin{aligned} \frac{dp}{dr} &= -\frac{G[M(r) + 4\pi r^3 p](\varepsilon + p)}{r[r - 2GM(r)]}, \\ \frac{dM}{dr} &= 4\pi\varepsilon r^2, \end{aligned} \tag{6}$$

where $r$ is the radial distance from the center, $M(r)$ is the enclosed mass of a neutron star within $r$, $\varepsilon$ represents the energy density, and $p$ the pressure. Figure 3 shows the mass and radius curves for the three different Skyrme parameter sets. For inhomogeneous nuclear matter in the crust of neutron stars, we used the EOS from the liquid drop model described in more detail in Sec. III.

The central shaded area is a comprehensive estimate of neutron star radii from observations of X-ray bursters [73]. The rectangular bars around $2.0M_\odot$ represent observational constraints on the maximum neutron star mass [74,75]. For all three Skyrme parametrizations we see that the maximum neutron star mass is equal to $2.1M_\odot$. Therefore, all of the parameter sets satisfy the maximum mass constraint and moreover are also consistent with the radius constraint. The speed of sound in nuclear matter is defined as

$$\frac{c_s^2}{c^2} = \frac{\partial p/\partial n}{\partial\varepsilon/\partial n}, \tag{7}$$

where $c$ is the speed of light. The speed of sound for the new Skyrme parametrizations was checked. The total baryon number densities when $c_s/c = 1$ are 1.41, 1.11, 1.50 fm$^{-3}$ for Sk$\chi$414, Sk$\chi$450, Sk$\chi$500 respectively. The central densities reached at maximum neutron star mass are 1.17, 1.18, 1.14 fm$^{-3}$ for Sk$\chi$414, Sk$\chi$450, Sk$\chi$500 in this order. Only the Sk$\chi$450 would lead to a violation of causality in neutron stars close to the upper mass limit. However, for all of the new Skyrme parametrizations, $2.1M_\odot$ neutron stars satisfying the causality constraint can be constructed.

## III. NEUTRON STAR CRUST EOS AND THE CORE-CRUST BOUNDARY

In the crust of neutron stars, a nucleus exists at the center of unit cell, called as Wigner-Seitz cell. Electrons are treated as a free relativistic gas that interacts with protons only through the Coulomb interaction. In the inner crust, neutrons drip out of heavy nuclei and form a dilute gas of interacting particles. As the baryon number density increases, heavy nuclei, neutrons, and electrons merge together to make homogeneous nuclear matter.

### A. Compressible liquid drop model

A phenomenological approach to study the neutron star inner crust equation of state is to utilize the liquid drop model (LDM) in the Wigner-Seitz cell approximation.

The energy density used to obtain the ground state of inhomogeneous nuclear matter in the crust of a neutron star can be written as

$$\varepsilon = u n_i f_i + \frac{\sigma(x_i) u d}{r_N} + 2\pi(n_i x_i e r_N)^2 u f_d(u) + (1-u) n_{no} f_{no}, \tag{8}$$

where $u$ is the filling factor (the fraction of space taken up by a heavy nucleus in the Wigner-Seitz cell), $n_i$ is the number density of heavy nuclei, $x_i$ is the proton fraction, $f_i$ represents the volume contribution to the energy per baryon in the heavy nucleus obtained from the new Skyrme parametrizations, $\sigma(x_i)$ is the surface tension as a function of the proton fraction, $r_N$ is the heavy nucleus radius, $n_{no}$ is the density of the unbound neutron gas, $f_{no}$ is the energy density of the neutron gas, and $f_d$ is a geometric function describing the Coulomb interaction [43] for different dimensions $d$. The surface tension is given explicitly by

$$\sigma(x) = \sigma_0 \frac{2^{\alpha+1} + q}{(1-x)^{-\alpha} + q + x^{-\alpha}}, \tag{9}$$

where $q$ parametrizes how quickly the surface tension decreases as a function of the proton fraction $x$. Larger values of $q$ correspond to more gradual decreases in the surface tension for neutron-rich nuclei. The parametrization of the surface tension in Eq. (9) avoids the problem of negative values that can occur for highly neutron-rich nuclei when a simple quadratic formula for the surface tension is used [76]. The numerical values of $\sigma_0$ and $q$ are fitted to give the lowest root-mean-square deviation to known nuclear masses [77]. For the three chiral interactions n3lo414, n3lo450, and n3lo500, we find $\sigma_0 = \{1.311, 1.186, 1.233\}$ MeV fm$^{-2}$ and $q = \{40.362, 46.748, 69.413\}$, respectively. In all cases $\alpha = 3.4$ is used since it is adequate in describing both isolated nuclei and nuclei in dense matter.

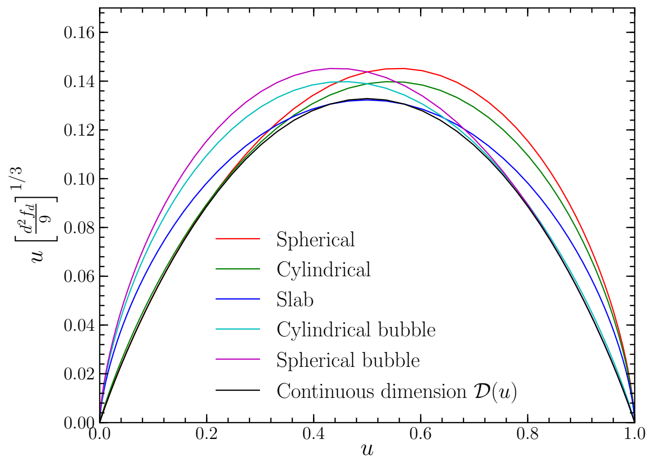

FIG. 4. Shape function $\mathcal{D}(u)$ for discrete dimension and continuous dimension. The continuous dimension curve always lies below those of the discrete geometries.

The Coulomb energies for different nuclear geometries (e.g., cylindrical or planar) are encoded in the function

$$f_d(u) = \frac{1}{d+2}\left[\frac{2}{d-2}\left(1 - \frac{1}{2} d u^{1-2/d}\right) + u\right]. \tag{10}$$

The case $d = 3$ corresponds to spherical shape, $d = 2$ to cylindrical shape, and $d = 1$ to slab shape. The equation for spherical bubble geometry can be obtained with the replacement $u\sigma \to (1-u)\sigma$ and $u f_d(u) \to (1-u) f_d(1-u)$. For a given baryon number density $n$ and proton fraction $Y_p$, we solve the following equations for the four unknowns $\{u, n_i, x_i, n_{no}\}$:

$$\mu_{ni} - \frac{x_i \sigma'(x_i) d}{r_N n_i} = \mu_{no}, \tag{11a}$$

$$P_i - 2\pi(n_i x_i e r_N)^2 \frac{\partial(u f_d)}{\partial u} = P_{no}, \tag{11b}$$

$$n - u n_i - (1-u) n_{no} = 0, \tag{11c}$$

$$n Y_p - u n_i x_i = 0, \tag{11d}$$

where $n$ is the total baryon number density in the Wigner-Seitz cell. From the nuclear virial theorem, the surface energy $E_S = \sigma(x_i) u d / r_N$ is related to the Coulomb energy $E_C = 2\pi(n_i x_i e r_N)^2 u f_d(u)$ by $E_S = 2E_C$, which is obtained by setting $\partial\varepsilon/\partial r_N = 0$. This gives [78] the relation $E_S + E_C = \beta\mathcal{D}$, where $\beta = (\frac{243\pi}{2})^{1/3}(n_i x_i e \sigma)^{2/3}$ and $\mathcal{D}(u) = u[\frac{d^2 f_d}{9}]^{1/3}$. If we allow $d$ to be continuous, we can find the shape function $\mathcal{D}$ that describes all pasta phases with a single formula.

We adopt the function $\mathcal{D}$ used in the Lattimer-Swesty EOS [78]:

$$\mathcal{D}(u) = u(1-u)\frac{(1-u) f_3^{1/3} + u f_3^{1/3}(1-u)}{u^2 + (1-u)^2 + 0.6u^2(1-u)^2}. \tag{12}$$

The combined pasta phase model can be implemented if a continuous dimension $d$ is allowed. Figure 4 shows the shape function $\mathcal{D}(u)$ for each discrete dimension (shown as colored lines) as well as for continuous dimension (black

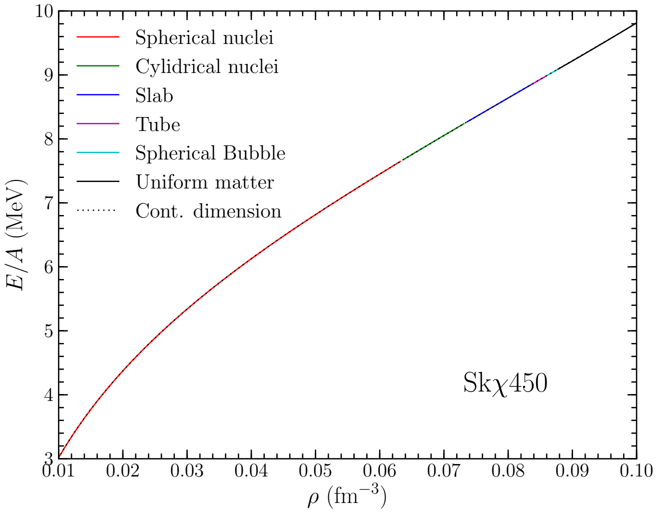

FIG. 5. Energy per nucleon as a function of baryon number density in beta-stable nuclear matter employing the liquid drop model with the Sk$\chi$450 Skyrme mean field model.

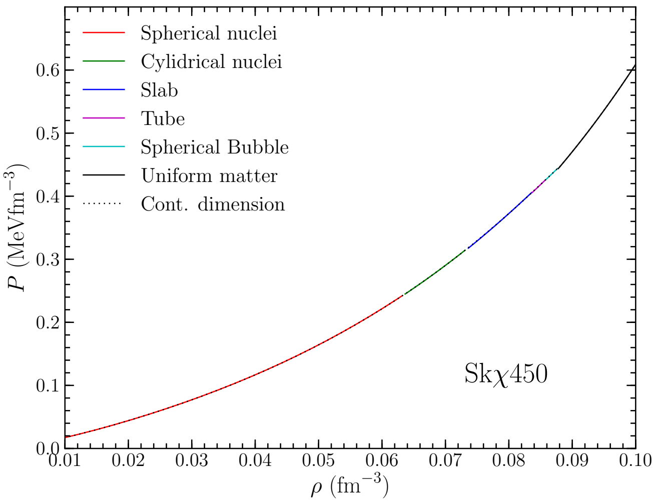

FIG. 6. Pressure as a function of baryon number density in beta-stable nuclear matter employing the liquid drop model with the Sk$\chi$450 Skyrme mean field model. At each transition density the pressure is almost continuous in the case of the LDM approach.

line). The latter has the correct behavior as $u \to 0$ and $u \to 1$. It represents the energy state that minimizes the combined Coulomb and surface energies.

Note that the dimension of the lowest energy state will be determined by the volume fraction of dense matter in the Wigner-Seitz cell. The crossing points for each dimension are independent of the equation of state and occur at the values $u = \{0.21525, 0.35499, 0.64501, 0.78475\}$ for the {3D-2D, 2D-1D, 1D-2DB, 2DB-3DB} transitions. For instance, if the volume fraction of dense matter is 0.4, then the lowest energy state is the slab phase.

In Fig. 5 we show the energy per baryon in the geometric configuration with the lowest energy, including also the beta-equilibrium condition. As the density increases the lowest energy state proceeds through $d = 3,2,1,2\text{B},3\text{B}$, and finally to uniform matter. By "2B" and "3B" we denote the two-dimensional and three-dimension bubble geometries. The solution found by employing a continuous dimension correctly represents the lowest energy state. The first derivative of $E/A$ with respect to the baryon number density, namely the pressure, is shown in Fig. 6. The pressure at each transition density is essentially continuous in the LDM formalism. The continuous dimension LDM also gives the correct numerical values compared with the discrete dimension calculation in the LDM.

In Table III we show the phase transition densities to different nuclear pasta geometries in the neutron star inner crust. We see that the different Sk$\chi$ mean field models predict similar transition densities for each of the phases, with uncertainties less than 0.006 fm$^{-3}$.

In Fig. 7 we show the volume fraction of dense matter in the Wigner-Seitz cell for each discrete dimension and continuous dimension calculation. The volume fractions for the lowest energy states are in the correct regions as expected. Therefore, the volume fraction of the dense phase in the Wigner-Seitz cell at each dimension can be used to identify the ground state dimension among the different pasta phases. The continuous dimension approach provides a reliable way to construct the nuclear equation of state in the pasta phase analytically. This also indicates that the supernova EOS table [78] using the continuous dimension is a valid numerical method that does not destroy the continuity in pressure at each transition density.

### B. Thomas-Fermi approximation

In the Thomas-Fermi (TF) approximation, the number density and momentum density are given by

$$\rho_t = \frac{1}{4\pi^2}\int_0^\infty f_t\, d^3p, \quad \tau_t = \frac{1}{4\pi^2}\int_0^\infty f_t\, p^2 d^3p \tag{13}$$

where $t$ is the type of nucleon and $f_t$ is the Fermi occupation function:

$$f_t = \frac{1}{1+\exp\left(\frac{\varepsilon_t-\mu_t}{T}\right)}, \tag{14}$$

where $\varepsilon_t$ is the single-particle energy for protons or neutrons and $\mu_t$ is the chemical potential for each species. At $T = 0$ MeV this equation simply gives $\tau_t = \frac{3}{5}(3\pi^2)^{2/3}\rho_t^{5/3}$. In the crust of neutron stars, the density profile of inhomogeneous

TABLE III. Transition densities (in units of fm$^{-3}$) between different geometries in the neutron star inner crust using the LDM method.

| | Sk$\chi$414 | Sk$\chi$450 | Sk$\chi$500 |
|---|---|---|---|
| 3DN-2DN | 0.0665 | 0.0634 | 0.0656 |
| 2DN-1DN | 0.0766 | 0.0736 | 0.0782 |
| 1DN-2DB | 0.0864 | 0.0837 | 0.0895 |
| 2DB-3DB | 0.0884 | 0.0859 | 0.0918 |
| 3DB-Uni. | 0.0901 | 0.0878 | 0.0940 |

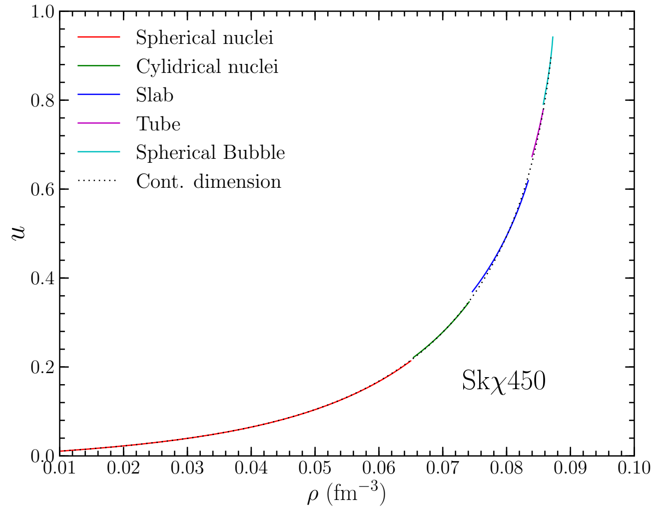

FIG. 7. Volume fraction of the dense phase in the Wigner-Seitz cell. The volume fraction indicates which dimension is the ground state for a given baryon number density.

nuclear matter can be parametrized [46] as

$$n_t(r)=\begin{cases}(n_{ti}-n_{to})\left[1-\left(\frac{r}{R_t}\right)^{\alpha_t}\right]^3+n_{to} & \text{if } r<R_t,\\ n_{to} & \text{if } r\geqslant R_t.\end{cases} \tag{15}$$

When $\mu_n>0$, $n_{no}\neq 0$. Thus $n_{no}$ represents the density of the unbound neutron gas. Depending on the density, all parameters ($n_{ti}$, $n_{to}$, $r_t$, $R_t$, $\alpha_t$) are to be obtained numerically from the minimization of the total energy:

$$E=\int[\mathcal{H}(n_n,n_p)+m_n n_n+m_p n_p+\mathcal{E}_{el}(n_e) + \mathcal{E}_{\rm Coul}(n_p,n_e)+\mathcal{E}_{ex}(n_p,n_e)]\,d\mathbf{r}, \tag{16}$$

where $\mathcal{E}_{el}$ is the energy density of noninteracting electrons and the Hamiltonian $\mathcal{H}$ is given by

$$\mathcal{H}(n_n,n_p)=\frac{1}{2m_n}\tau_n+\frac{1}{2m_p}\tau_p+V_{NN}(n_n,n_p). \tag{17}$$

We use for $V_{NN}$ the nonrelativistic Skyrme force models obtained in this work. In the crust of neutron stars, the electrons are distributed uniformly, so we assume a constant electron density. The Coulomb energy is given by

$$\mathcal{E}_{\rm Coul}(n_p,n_e)=\tfrac{1}{2}[n_p(r)-n_e][V_p(r)-V_e(r)]. \tag{18}$$

The Coulomb potentials for protons and electrons are given by

$$V_p(\mathbf{r})=\int\frac{e^2\,n_p(\mathbf{r}')}{|\mathbf{r}-\mathbf{r}'|}\,d\mathbf{r}',\quad V_e(\mathbf{r})=\int\frac{e^2\,n_e}{|\mathbf{r}-\mathbf{r}'|}\,d\mathbf{r}' \tag{19}$$

and the Coulomb exchange energy is given as [79]

$$\mathcal{E}_{ex}=-\frac{3}{4}\left(\frac{3}{\pi}\right)^{1/3}e^2\left[n_p^{4/3}(\mathbf{r})+\Phi(x_e)n_e^{4/3}\right], \tag{20}$$

where

$$\Phi(x_e)=\frac{1}{4x_e^4}\left[\frac{9}{4}+3\left(\beta^2-\frac{1}{\beta^2}\right)\ln\beta-6(\ln\beta)^2 -\left(\beta^2+\frac{1}{\beta^2}\right)-\frac{1}{8}\left(\beta^4+\frac{1}{\beta^4}\right)\right],$$
$$x_e=\frac{k_{F_e}}{m_e c};\quad \beta=x_e+\sqrt{1+x_e^2}. \tag{21}$$

Note that $x_e\ll 1$ indicates a nonrelativistic limit and thus $\Phi(x_e)$ approaches 1. On the other hand, when $x_e\gg 1$, $\Phi(x_e)$ becomes $-1/2$, which changes the sign and thus the exchange interaction becomes repulsive compared with the nonrelativistic case. We take $\Phi(x_e)=-1/2$ since $x_e\geqslant 80$ in the inner crust of neutron stars. The nuclear pasta phases require Coulomb interaction formulas for different dimensions [51]:

Spherical:

$$V_p(r)=4\pi e^2\left[\frac{1}{r}\int_0^r r'^2\rho_p(r')dr'+\int_r^{R_c} r'\rho_p(r')dr'\right],$$
$$V_e(r)=2\pi e^2 n_e\left[R_c^2-\frac{1}{3}r^2\right]. \tag{22}$$

Cylindrical:

$$V_p(r)=-4\pi e^2\left[\ln(r)\int_0^r r'\rho_p(r')dr' +\int_r^{R_c} r'\ln r'\rho_p(r')dr'\right],$$
$$V_e(r)=\pi e^2 n_e R_c^2\left[1-\frac{r^2}{R_c^2}-2\ln R_c\right]. \tag{23}$$

Slab:

$$V_p(z)=-4\pi e^2\left[z\int_0^z \rho_p(z')dz'+\int_z^{R_c} z'\rho_p(z')dz'\right],$$
$$V_e(z)=-2\pi e^2 n_e\left(z^2+R_c^2\right). \tag{24}$$

Figure 8 shows the energy per baryon for beta-equilibrated neutron star matter obtained in the TF approximation using the Skyrme parametrization Skχ450 developed in the present work. As in the case of the LDM model, the ground-state geometry for increasing density proceeds through the sequence {spherical, cylindrical, slab, cylindrical hole, spherical hole, uniform matter} in this order. Each new geometry spans smaller and smaller ranges of densities, and the transition density to the homogeneous phase occurs at $n_c=0.084\ \text{fm}^{-3}$.

The ground state pressure as a function of density employing the same interaction model is shown in Fig. 9. Unlike the LDM approach, the Thomas-Fermi approximation results in a small discontinuity in the pressure at the interface between each phase when we only compare the energy per baryon to find the ground state of the phase. This is caused by the intrinsic discontinuity in the expressions for the Coulomb energy in the different geometries. The LDM approach enables us to investigate the structure of the pasta phase with fewer parameters, so the pressure discontinuity or proton fraction discontinuity can be small. On the other hand, the more

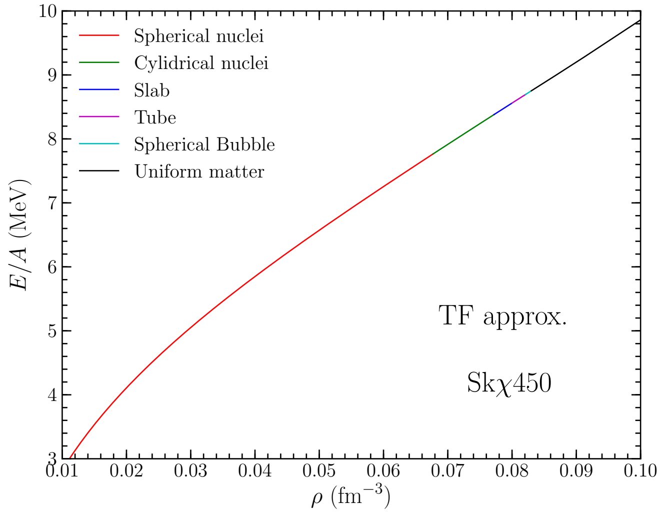

FIG. 8. Energy per baryon using the TF approximation with the Sk$\chi$450 Skyrme fit model.

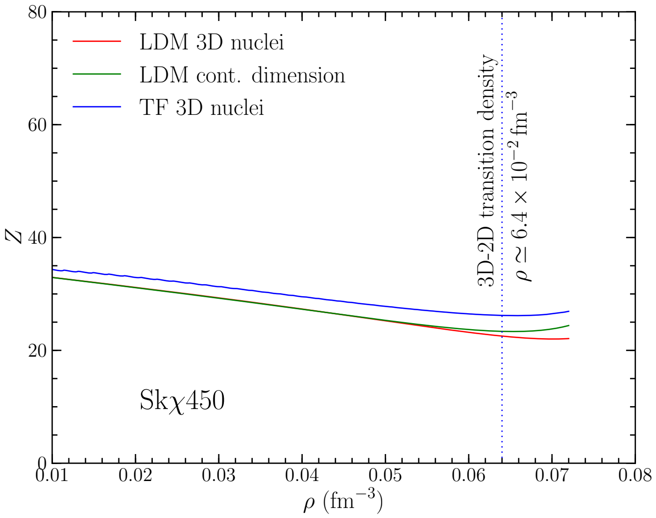

FIG. 10. Atomic number of heavy nucleus in the Wigner Seitz cell. The dotted line around $\rho = 0.064$ fm$^{-3}$ indicates the transition between 3D nuclei and 2D nuclei.

realistic TF method can be performed in space discretization. This means that the discontinuity in the pressure is a natural phenomenon in the case of phase transformation in the TF approximation. When the Maxwell construction is employed, the interval of the density in the coexistence region is so small ($\Delta\rho = 0.0001$ fm$^{-3}$) that the microscopic structure of the neutron star barely changes. As an example, the two densities of mixed state for spherical shape and cylindrical shape are $\rho_{t_1} = 0.06406$ fm$^{-3}$ and $\rho_{t_2} = 0.06414$ fm$^{-3}$.

The choice of LDM vs TF model also gives rise to differences in nuclear composition. Figure 10 shows the atomic number of heavy nuclei in the crust of neutron stars. We define the atomic number as the integrated number of protons in the Wigner-Seitz cell. The dotted line indicates the 3D–2D phase transition density, which is nearly independent of whether we employ the LDM or the TF model. The atomic number is consistently larger in the TF approximation, differing from the LDM atomic number by roughly 2 up to the transition to cylindrical geometry. The atomic number in continuous dimension over the 3D–2D phase transition density represents the average atomic number in the unit cell. It is not a physical quantity in the crust. Above the 3D–2D phase transition density, the TF model gives a larger atomic number since the Wigner-Seitz cell decreases as the total baryon density increases (which means the distance between nuclei decreases) and total number of protons and neutrons increases in the spherical cell.

Figure 11 shows the neutron and proton density profiles in each numerical calculation with the Sk$\chi$450 interaction. Even if the central densities of protons and neutrons are different

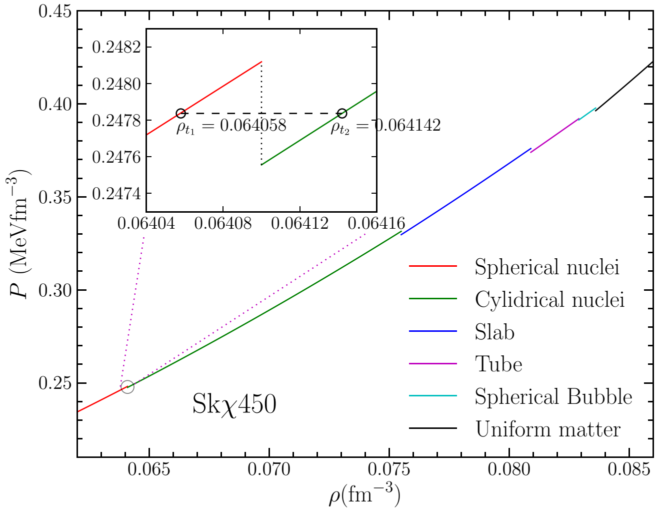

FIG. 9. Pressure vs baryon number density using in the TF approximation. A discontinuity in the pressure occurs at the shape transition densities, but the discontinuity region (shown in the inset) is very narrow.

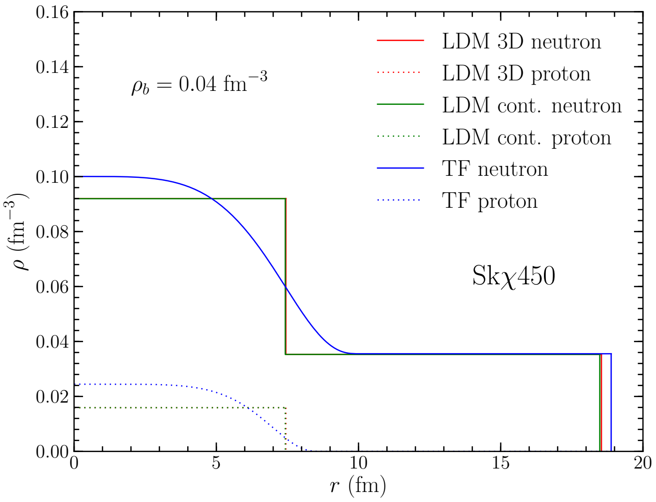

FIG. 11. Neutron and proton density profiles using three different numerical methods with the Sk$\chi$450 Skyrme mean field model.

TABLE IV. Pasta phase transition densities (in units of $\mathrm{fm}^{-3}$) using the TF method. The numbers in parentheses represent the transition densities with the exchange Coulomb interaction included.

| | Sk$\chi$414 | Sk$\chi$450 | Sk$\chi$500 |
|---|---|---|---|
| 3DN-2DN | 0.0681 | 0.0641 | 0.0626 |
| | (0.0684) | (0.0643) | (0.0629) |
| 2DN-1DN | 0.0791 | 0.0755 | 0.0790 |
| | (0.0795) | (0.0759) | (0.0795) |
| 1DN-2DB | 0.0830 | 0.0809 | 0.0865 |
| | (0.0830) | (0.816) | (0.0868) |
| 2DB-3DB | 0.0852 | 0.0830 | 0.0885 |
| | (0.0860) | (0.0835) | (0.0890) |
| 3DB-Uni. | 0.0860 | 0.0835 | 0.0894 |
| | (0.0868) | (0.0842) | (0.0894) |

in the LDM and TF model, the neutron densities outside the nucleus are nearly the same. This indicates that the density profile is the problem to be solved in order to understand the coexistence of dense and dilute matter. Whatever numerical method is used, the density of the unbound gas of neutrons should be the same under identical physical conditions.

Table IV shows the transition density at each phase boundary. The transition density for uniform matter is highly correlated with the saturation density. If the saturation density is greater (as is the case for the Sk$\chi$414 and Sk$\chi$500 Skyrme interactions), uniform nuclear matter is formed at a higher density. The numbers in parentheses indicate the transition density when we include the exchange Coulomb interaction in the numerical calculation. The exchange Coulomb interaction in Eq. (20) gives a negative contribution to the total energy and therefore its presence tends to delay the transitions to higher densities. However, the effects are nearly negligible.

### C. Thermodynamic instability

In neutron stars, the phase transition from uniform nuclear matter to inhomogeneous nuclear matter takes place when matter begins to exhibit an instability to density fluctuations. Baym *et al.* [80] show that the matter is stable when the following relationship is maintained:

$$v_0 + 2(4\pi e^2\beta)^{1/2} - \beta k_{TF}^2 > 0, \tag{25}$$

where

$$v_0 = \frac{\partial\mu_p}{\partial\rho_p} - \frac{(\partial\mu_p/\partial\rho_n)^2}{\partial\mu_n/\partial\rho_n}, \tag{26}$$

$$\beta = 2(Q_{pp} + 2Q_{np}\zeta + Q_{nn}\zeta^2), \quad \zeta = -\frac{\partial\mu_p/\partial\rho_n}{\partial\mu_n/\partial\rho_n}, \tag{27}$$

and $k_{TF}$ is the Thomas-Fermi wave number,

$$k_{TF}^2 = \frac{4e^2}{\pi}k_e^2, \quad k_e = (3\pi^2\rho_p)^{1/3}. \tag{28}$$

In Skyrme models, $Q_{nn}$ and $Q_{np}$ are given by

$$\begin{aligned} Q_{nn} &= Q_{pp} = \tfrac{3}{16}[t_1(1-x_1) - t_2(1+x_2)], \\ Q_{np} &= Q_{pn} = \tfrac{1}{16}[3t_1(2+x_1) - t_2(2+x_2)]. \end{aligned} \tag{29}$$

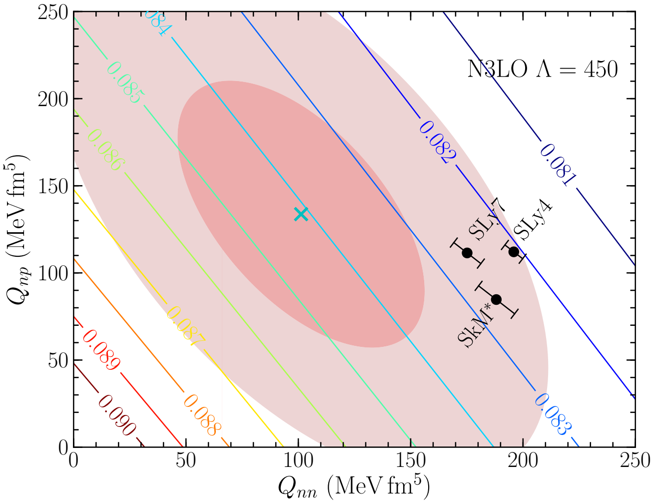

FIG. 12. Transition density contour plot for the core-crust boundary obtained from thermodynamic instability. The individual points are taken from the modified Skyrme interactions obtained in Ref. [81].

For the three Skyrme parametrizations developed in this work, $Q_{nn}$ and $Q_{np}$ are given by $Q_{nn} = \{107.297, 105.458, 106.901\}$ MeV fm$^5$ and $Q_{np} = \{119.833, 94.759, 119.641\}$ MeV fm$^5$ for Sk$\chi$414, Sk$\chi$450, and Sk$\chi$500 respectively. A more conservative uncertainty estimate is obtained by considering a wider set of 31 Skyrme models whose neutron matter equations of state are similar to that from chiral effective field theory. The 31 Skyrme force models include KDE [82], KDE0 [82], LNS [83], MSk1 [84], MSk2 [84], SGII [85], SkM [86], SkM* [87], SkT1 [88], SkT2 [88], SkT3 [88], SkT8 [88], SKX [89], SKXce [89] Skxs15 [90], Skz-1 [91], SLy0 [92], SLy1 [92], SLy2 [92], SLy3 [93], SLy4 [93], SLy5 [93], SLy6 [93], SLy7 [93], SLy8 [92], SLy9 [92], SLy10 [93], SLy230a [94], UNEDF0 [95], and UNEDF1 [96]. Figure 12 shows the resulting confidence contour of $Q_{nn}$ and $Q_{np}$, with the symbol "×" at the center of the ellipse representing the average values. In these calculations the proton and neutron chemical potentials in homogeneous matter are taken from the microscopic equation of state computed from the $\Lambda = 450$ MeV chiral nuclear potential. The three individual points labeled "SLy7," "SLy4," and "SkM*" come from the modified isovector gradient coupling strengths deduced in recent quantum Monte Carlo studies [81]. Figure 12 indicates that the density for the core-crust boundary is between $\rho = 0.082\ \mathrm{fm}^{-3}$ and $\rho = 0.087\ \mathrm{fm}^{-3}$. We infer from the contour plot that the core-crust transition density is proportional to the sum of $Q_{nn} + kQ_{np}$. We propose an empirical formula for the core-crust density with $Q_{nn}$ and $Q_{np}$:

$$\rho_t \simeq \rho_{t_1} + \alpha Q_{nn} + \beta Q_{np}, \tag{30}$$

which indicates that $Q_{nn}$ and $Q_{np}$ will directly determine the core-crust density. Table V shows $\alpha$ and $\beta$ corresponding to Eq. (30), which were obtained from our new parametrization.

TABLE V. Numerical values for the parameters in Eq. (30).

| | |
|---|---|
| $\rho_{t_1}$ (fm$^{-3}$) | $9.103 \times 10^{-2} \pm 7.065 \times 10^{-4}$ |
| $\alpha$ (MeV$^{-1}$ fm$^{-8}$) | $-3.088 \times 10^{-5} \pm 5.257 \times 10^{-7}$ |
| $\beta$ (MeV$^{-1}$ fm$^{-8}$) | $-1.891 \times 10^{-5} \pm 1.010 \times 10^{-6}$ |

## IV. CONCLUSION

We have studied the composition and structure of neutron star crusts by comparing the energy densities for different pasta phases using both the liquid drop model and the Thomas-Fermi model. The results are based on a new set of extended Skyrme parametrizations derived in the present work that fit the bulk isospin-asymmetric nuclear matter equation of state from $\chi$EFT and the binding energies of doubly-magic nuclei. The neutron star maximum masses obtained from these Skyrme parametrizations are consistent with observations of $2.0M_\odot$ neutron stars.

From the LDM and TF calculations, the crust-core transition density is strongly correlated with the saturation density of symmetric nuclear matter. For this reason the extended Skyrme parametrization Sk$\chi$450, which reproduces well both the empirical saturation energy and density, is expected to provide the most reliable prediction for the crust-core interface density. The predicted pressure at the phase boundaries between different pasta geometries is smooth in the LDM but exhibits small discontinuities in the TF approximation. We have studied as well a continuous-dimension LDM that treats the pasta phases as a function of the dense matter volume fraction in the Wigner-Seitz cell. All three methods give a core-crust boundary density around half saturation density, $\rho_t = 0.084$ fm$^{-3}$.

Compared to previous works [97,98], we analyzed the theoretical uncertainties in the core transition density of neutron stars by varying the gradient terms $Q_{nn}$ and $Q_{np}$. We find that the transition density has a two-dimensional correlation with the $Q$'s. Low values of these gradient term coupling strengths result in an increase in the transition density from the crust to core, which increases the volume of the neutron star crust. The uncertainty in $Q_{nn}$ and $Q_{np}$ can be reduced by microscopic calculations of the static density response function using $\chi$EFT in many-body perturbation theory or quantum Monte Carlo simulations. A more accurate determination of $Q_{nn}$ and $Q_{np}$ will therefore play an important role for improving energy density functionals and to more accurately predict the density at a neutron star's core-crust boundary.

We find that nuclear pasta exists within the density range between $\rho = 0.065$ and $0.090$ fm$^{-3}$. Macroscopically it exists within a 100 m thickness in the inner crust of a neutron star with $1.4M_\odot$. The spherical hole phase exists within the density range of $\Delta\rho = 0.002$ fm$^{-3}$ at most. This means that spherical holes exist only within a $\Delta R = 5$ m range in neutron stars, which might be destroyed in fast rotating neutron stars because of tidal deformation. Our results are similar to the previous works of Oyamatsu [46] and Sharma *et al.* [51], who employed phenomenological models with equations of state similar to the predictions from $\chi$EFT.

---

[1] F. Weber, Prog. Part. Nucl. Phys. **54**, 193 (2005).
[2] M. Alford, M. Braby, M. Paris, and S. Reddy, Astrophys. J. **629**, 969 (2005).
[3] S. Weissenborn, I. Sagert, G. Pagliara, M. Hempel, and J. Schaffner-Bielich, Astrophys. J. **740**, L14 (2011).
[4] J. Schaffner-Bielich, M. Hanauske, H. Stöcker, and W. Greiner, Phys. Rev. Lett. **89**, 171101 (2002).
[5] S. Weissenborn, D. Chatterjee, and J. Schaffner-Bielich, Nucl. Phys. A **881**, 62 (2012).
[6] S. Weissenborn, D. Chatterjee, and J. Schaffner-Bielich, Phys. Rev. C **85**, 065802 (2012); **90**, 019904(E) (2014).
[7] Y. Lim, C. H. Hyun, K. Kwak, and C.-H. Lee, Int. J. Mod. Phys. E **24**, 1550100 (2015).
[8] D. Chatterjee and I. Vidaña, Eur. Phys. J. A **52**, 29 (2016).
[9] G. Baym, Phys. Rev. Lett. **30**, 1340 (1973).
[10] V. Thorsson, M. Prakash, and J. M. Lattimer, Nucl. Phys. A **572**, 693 (1994).
[11] N. K. Glendenning and J. Schaffner-Bielich, Phys. Rev. Lett. **81**, 4564 (1998).
[12] Y. Lim, K. Kwak, C. H. Hyun, and C.-H. Lee, Phys. Rev. C **89**, 055804 (2014).
[13] S. Weinberg, Physica A **96**, 327 (1979).
[14] E. Epelbaum, H.-W. Hammer, and U.-G. Meißner, Rev. Mod. Phys. **81**, 1773 (2009).
[15] R. Machleidt and D. R. Entem, Phys. Rep. **503**, 1 (2011).
[16] E. Epelbaum, H. Krebs, and U.-G. Meißner, Eur. Phys. J. A **51**, 53 (2015).
[17] D. R. Entem, N. Kaiser, R. Machleidt, and Y. Nosyk, Phys. Rev. C **91**, 014002 (2015).
[18] E. Epelbaum, H. Krebs, D. Lee, and U. G. Meißner, Eur. Phys. J. A **40**, 199 (2009).
[19] K. Hebeler and A. Schwenk, Phys. Rev. C **82**, 014314 (2010).
[20] K. Hebeler, S. K. Bogner, R. J. Furnstahl, A. Nogga, and A. Schwenk, Phys. Rev. C **83**, 031301 (2011).
[21] L. Coraggio, J. W. Holt, N. Itaco, R. Machleidt, and F. Sammarruca, Phys. Rev. C **87**, 014322 (2013).
[22] A. Gezerlis, I. Tews, E. Epelbaum, S. Gandolfi, K. Hebeler, A. Nogga, and A. Schwenk, Phys. Rev. Lett. **111**, 032501 (2013).
[23] I. Tews, T. Krüger, K. Hebeler, and A. Schwenk, Phys. Rev. Lett. **110**, 032504 (2013).
[24] L. Coraggio, J. W. Holt, N. Itaco, R. Machleidt, L. E. Marcucci, and F. Sammarruca, Phys. Rev. C **89**, 044321 (2014).
[25] A. Roggero, A. Mukherjee, and F. Pederiva, Phys. Rev. Lett. **112**, 221103 (2014).
[26] G. Wlazłowski, J. W. Holt, S. Moroz, A. Bulgac, and K. J. Roche, Phys. Rev. Lett. **113**, 182503 (2014).
[27] A. Carbone, A. Rios, and A. Polls, Phys. Rev. C **90**, 054322 (2014).
[28] I. Tews, S. Gandolfi, A. Gezerlis, and A. Schwenk, Phys. Rev. C **93**, 024305 (2016).
[29] C. Drischler, V. Somà, and A. Schwenk, Phys. Rev. C **89**, 025806 (2014).
[30] C. Wellenhofer, J. W. Holt, and N. Kaiser, Phys. Rev. C **93**, 055802 (2016).

[31] L. Tolos, B. Friman, and A. Schwenk, Nucl. Phys. A **806**, 105 (2008).

[32] C. Wellenhofer, J. W. Holt, N. Kaiser, and W. Weise, Phys. Rev. C **89**, 064009 (2014).

[33] C. Wellenhofer, J. W. Holt, and N. Kaiser, Phys. Rev. C **92**, 015801 (2015).

[34] S. K. Bogner, R. J. Furnstahl, and L. Platter, Eur. Phys. J. A **39**, 219 (2009).

[35] J. W. Holt, N. Kaiser, and W. Weise, Eur. Phys. J. A **47**, 128 (2011).

[36] N. Kaiser, Eur. Phys. J. A **48**, 36 (2012).

[37] S. Gandolfi, J. Carlson, and S. C. Pieper, Phys. Rev. Lett. **106**, 012501 (2011).

[38] M. Buraczynski and A. Gezerlis, Phys. Rev. Lett. **116**, 152501 (2016).

[39] G. I. Lykasov, C. J. Pethick, and A. Schwenk, Phys. Rev. C **78**, 045803 (2008).

[40] D. Davesne, J. W. Holt, A. Pastore, and J. Navarro, Phys. Rev. C **91**, 014323 (2015).

[41] J. W. Holt, N. Kaiser, and W. Weise, Nucl. Phys. A **876**, 61 (2012).

[42] J. W. Holt, N. Kaiser, and W. Weise, Phys. Rev. C **87**, 014338 (2013).

[43] D. G. Ravenhall, C. J. Pethick, and J. R. Wilson, Phys. Rev. Lett. **50**, 2066 (1983).

[44] F. Douchin and P. Haensel, Astron. Astrophys. **380**, 151 (2001).

[45] W. G. Newton, M. Gearheart, and B.-A. Li, Astrophys. J. Suppl. Ser. **204**, 9 (2013).

[46] K. Oyamatsu, Nucl. Phys. A **561**, 431 (1993).

[47] M. Okamoto, T. Maruyama, K. Yabana, and T. Tatsumi, Phys. Rev. C **88**, 025801 (2013).

[48] F. Grill, H. Pais, C. Providência, I. Vidaña, and S. S. Avancini, Phys. Rev. C **90**, 045803 (2014).

[49] J. M. Pearson, N. Chamel, A. Pastore, and S. Goriely, Phys. Rev. C **91**, 018801 (2015).

[50] N. Martin and M. Urban, Phys. Rev. C **92**, 015803 (2015).

[51] B. K. Sharma, M. Centelles, X. Viñas, M. Baldo, and G. F. Burgio, Astron. Astrophys. **584**, A103 (2015).

[52] P. Gögelein and H. Müther, Phys. Rev. C **76**, 024312 (2007).

[53] W. G. Newton and J. R. Stone, Phys. Rev. C **79**, 055801 (2009).

[54] H. Pais and J. R. Stone, Phys. Rev. Lett. **109**, 151101 (2012).

[55] B. Schuetrumpf and W. Nazarewicz, Phys. Rev. C **92**, 045806 (2015).

[56] C. J. Horowitz, M. A. Pérez-García, D. K. Berry, and J. Piekarewicz, Phys. Rev. C **72**, 035801 (2005).

[57] H. Sonoda, G. Watanabe, K. Sato, K. Yasuoka, and T. Ebisuzaki, Phys. Rev. C **77**, 035806 (2008).

[58] A. S. Schneider, C. J. Horowitz, J. Hughto, and D. K. Berry, Phys. Rev. C **88**, 065807 (2013).

[59] B. A. Brown and A. Schwenk, Phys. Rev. C **89**, 011307 (2014).

[60] A. Bulgac, M. M. Forbes, and S. Jin, arXiv:1506.09195.

[61] E. Rrapaj, A. Roggero, and J. W. Holt, Phys. Rev. C **93**, 065801 (2016).

[62] D. R. Entem and R. Machleidt, Phys. Rev. C **68**, 041001 (2003).

[63] J. W. Holt and N. Kaiser, Phys. Rev. C **95**, 034326 (2017).

[64] J. W. Holt, N. Kaiser, and W. Weise, Prog. Part. Nucl. Phys. **73**, 35 (2013).

[65] J. W. Holt, M. Rho, and W. Weise, Phys. Rep. **621**, 2 (2016).

[66] J. B. Elliott, P. T. Lake, L. G. Moretto, and L. Phair, Phys. Rev. C **87**, 054622 (2013).

[67] T. Skyrme, Nucl. Phys. **9**, 615 (1958).

[68] D. Vautherin and D. M. Brink, Phys. Rev. C **5**, 626 (1972).

[69] M. Bender, P.-H. Heenen, and P.-G. Reinhard, Rev. Mod. Phys. **75**, 121 (2003).

[70] G. Audi *et al.*, At. Data Nucl. Data Tables **103**, 1 (2015).

[71] M. Dutra, O. Lourenço, J. S. Sá Martins, A. Delfino, J. R. Stone, and P. D. Stevenson, Phys. Rev. C **85**, 035201 (2012).

[72] H. De Vries, C. W. De Jager, and C. De Vries, At. Data Nucl. Data Tables **36**, 495 (1987).

[73] A. W. Steiner, J. M. Lattimer, and E. F. Brown, Astrophys. J. **722**, 33 (2010).

[74] P. Demorest, T. Pennucci, S. Ransom, M. Roberts, and J. Hessels, Nature **467**, 1081 (2010).

[75] J. Antoniadis *et al.*, Science **340**, 6131 (2013).

[76] D. G. Ravenhall, C. J. Pethick, and J. M. Lattimer, Nucl. Phys. A **407**, 571 (1983).

[77] M. Wang, G. Audi, A. Wapstra, F. Kondev, M. MacCormick, X. Xu, and B. Pfeiffer, Chin. Phys. C **36**, 1603 (2012).

[78] J. M. Lattimer and F. D. Swesty, Nucl. Phys. A **535**, 331 (1991).

[79] E. E. Salpeter, Astrophys. J. **134**, 669 (1961).

[80] G. Baym, H. A. Bethe, and C. Pethick, Nucl. Phys. A **175**, 225 (1971).

[81] M. Buraczynski and A. Gezerlis, Phys. Rev. C **95**, 044309 (2017).

[82] B. K. Agrawal, S. Shlomo, and V. K. Au, Phys. Rev. C **72**, 014310 (2005).

[83] L. G. Cao, U. Lombardo, C. W. Shen, and N. V. Giai, Phys. Rev. C **73**, 014313 (2006).

[84] F. Tondeur, S. Goriely, J. M. Pearson, and M. Onsi, Phys. Rev. C **62**, 024308 (2000).

[85] N. V. Giai and H. Sagawa, Phys. Lett. B **106**, 379 (1981).

[86] H. Krivine, J. Treiner, and O. Bohigas, Nucl. Phys. A **336**, 155 (1980).

[87] J. Bartel, P. Quentin, M. Brack, C. Guet, and H.-B. Hkansson, Nucl. Phys. A **386**, 79 (1982).

[88] F. Tondeur, M. Brack, M. Farine, and J. Pearson, Nucl. Phys. A **420**, 297 (1984).

[89] B. A. Brown, Phys. Rev. C **58**, 220 (1998).

[90] B. A. Brown, G. Shen, G. C. Hillhouse, J. Meng, and A. Trzcińska, Phys. Rev. C **76**, 034305 (2007).

[91] J. Margueron, J. Navarro, and N. V. Giai, Phys. Rev. C **66**, 014303 (2002).

[92] E. Chabanat, Ph.D. thesis, University of Lyon, 1995 (unpublished).

[93] E. Chabanat, P. Bonche, P. Haensel, J. Meyer, and R. Schaeffer, Nucl. Phys. A **635**, 231 (1998).

[94] E. Chabanat, P. Bonche, P. Haensel, J. Meyer, and R. Schaeffer, Nucl. Phys. A **627**, 710 (1997).

[95] M. Kortelainen, T. Lesinski, J. Moré, W. Nazarewicz, J. Sarich, N. Schunck, M. V. Stoitsov, and S. Wild, Phys. Rev. C **82**, 024313 (2010).

[96] M. Kortelainen, J. McDonnell, W. Nazarewicz, P.-G. Reinhard, J. Sarich, N. Schunck, M. V. Stoitsov, and S. M. Wild, Phys. Rev. C **85**, 024304 (2012).

[97] K. Hebeler, J. M. Lattimer, C. J. Pethick, and A. Schwenk, Astrophy. J. **773**, 11 (2013).

[98] I. Tews, Phys. Rev. C **95**, 015803 (2017).